

An Anatomy-Aware Shared Control Approach for Assisted Teleoperation of Lung Ultrasound Examinations

Davide Nardi¹, Edoardo Lamon¹, Luca Beber¹, Daniele Fontanelli², Matteo Saveriano², and Luigi Palopoli¹

Abstract—The introduction of artificial intelligence and robotics in telehealth is enabling personalised treatment and supporting teleoperated procedures such as lung ultrasound, which has gained attention during the COVID-19 pandemic. Although fully autonomous systems face challenges due to anatomical variability, teleoperated systems appear to be more practical in current healthcare settings. This paper presents an anatomy-aware control framework for teleoperated lung ultrasound. Using biomechanically accurate 3D models such as SMPL and SKEL, the system provides a real-time visual feedback and applies virtual constraints to assist in precise probe placement tasks. Evaluations on five subjects show the accuracy of the biomechanical models and the efficiency of the system in improving probe placement and reducing procedure time compared to traditional teleoperation. The results demonstrate that the proposed framework enhances the physician’s capabilities in executing remote lung ultrasound examinations, towards more objective and repeatable acquisitions.

I. INTRODUCTION

The incorporation of data-driven approaches into telehealth devices enhances their predictive capabilities by assisting clinicians in diagnosis and recommendations, towards personalised treatment plans also based on real-time patient data. In addition, progress in robotics, haptics, and virtual reality is simplifying remote visits and surgeries, where a physician can examine or operate a patient in a different location using robotic instruments controlled via a telehealth interface. The COVID-19 pandemics further underscored the critical role of telehealth in maintaining healthcare access and preventing the spread of infectious diseases, while also opening to new research challenges. In particular, in the context of lung ultrasound, researchers have focused on developing standardised procedures [1], [2] and enhancing both teleoperated [3]–[5] and autonomous [6]–[8] robotic ultrasound technologies based on collaborative manipulators. Due to the significant anatomical variability across individuals, fully autonomous systems remain a considerable challenge and are not yet ready for widespread implementation in hospitals and healthcare facilities. Telepresence and teleoperated robotic systems, instead, have proven to be effective solutions, especially in cases where human decision-making capabilities are still superior to the level of autonomy reached by the intelligence of such systems. However, physical telehealth systems require trained experts capable of not only operating

remotely machines but also replicating complex medical procedures. Due to these constraints, the number of experts is usually limited and below demand. For this reason, user-friendliness and the ability to provide reliable feedback [9], assist [10] and train [11] the operator are of paramount importance. Virtual fixtures (VF) are one of the widely used tools to provide assistance to a remote operator in a shared control fashion, by constraining a teleoperated robot to stay within/avoid certain regions in space [12]. Although initial approaches envisioned the prior computations of such regions, which is not always feasible, more recent ones tried to exploit visual data [13], [14] and point clouds [15] to initialise them. However, these methods assume that the constrained region is always directly measurable and can be sensed with cameras.

In lung ultrasound, the probe should be placed in the intercostal areas [1], [2] to avoid the shadowing effect due to the presence of the ribs [16]. Detecting the bones and thus placing the probe, mounted on the end effector of the manipulator, in such a narrow area could become a complex task, especially in the case of teleoperated robotic ultrasound exams, where standard visual and haptic feedback, fundamental in in-person exams, might not suffice. One of the main issues arises when the robot is in close proximity to the patient. In such a case, the patient’s view captured by a fixed RGB camera might be occluded by the robot. If the camera is mounted on the robot’s end effector, instead, it might be too close to the patient with a limited field of view. In such a case, a dynamic 3D model, which includes the anatomical features of the patient, such as the rib cage in the case of lung ultrasound, and the target pose of the robot might provide great support. Also, when the probe is in contact with the body, with standard haptic feedback, it is not easy to distinguish if the probe is located on top of a bone or a soft tissue and thus the practitioner should rely mainly on the ultrasound image. Another issue is represented by the low repeatability and the high subjectivity of the operations, as the success of the exam depends very much on the practitioner’s ability.

To overcome these limitations and assist the physician in the teleoperation tasks, we present in this manuscript an anatomy-aware shared control framework for lung ultrasound examination, which leverages novel biomechanically accurate 3D digital models, such as SMPL [17] and SKEL [18] to generate reliable 3D visual feedback for the human operator and define the end-effector forbidden regions that are enforced by the presence of VF. In this way, the physician is assisted in two ways: i) in wide robot motions, such as

We acknowledge the support of the MUR PNRR project FAIR - Future AI Research (PE00000013) and the project iNEST - Interconnected Nord-Est Innovation Ecosystem (ECS 00000043) funded by the NextGenerationEU.

¹Department of Information Engineering and Computer Science, Università di Trento, Trento, Italy. edoardo.lamon@unitn.it

²Department of Industrial Engineering, Università di Trento, Trento, Italy.

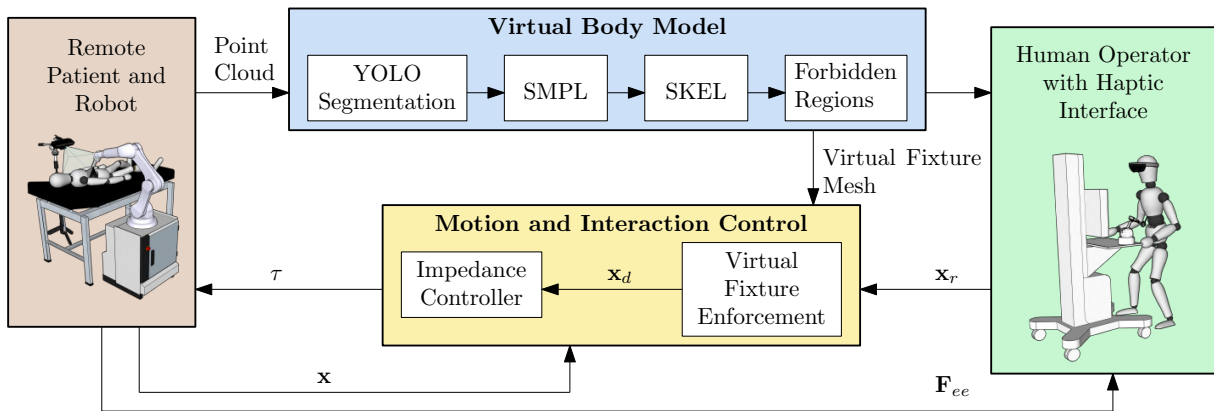


Fig. 1. High level overview of the proposed framework.

the reach of the target areas, through the anatomical 3D visual feedback, which ease the task of finding the desired probe placement, and ii) in the fine-grained placements on the intercostal area, thanks to the presence of the VF, which forbids the probe to end up on the ribs. The framework (Figure 1) consists of two main components: the generation of the patient’s 3D virtual body model and the enforcement of the VF on the reference coming from the haptic device controlled by the physician. In the first part, the coloured pointcloud of the patient is filtered thanks to the accurate human segmentation provided by YOLOv8-seg [19] and then fitted through regression to a SMPL model that approximates the volumetric occupancy of the body of the patient. Based on the SMPL model, a biomechanical skeletal model (SKEL) is generated. The rib cage is then projected and elaborated on the SMPL to define the forbidden regions. The resulting mesh is passed to a constraint programme that enforces the VF onto the reference position of the haptic interface. The filtered position is then transmitted to the interaction controller, which regulates the motion of the robot. The force and torque exerted by the robot on the environment, measured at the end effector, are transmitted back to the haptic interface, providing the physician with tactile feedback to indicate contact with the patient’s body. The proposed framework is evaluated on a proof-of-concept teleoperated lung ultrasound examination procedure. We performed the exam on male healthy subjects, and we assessed three different aspects: i) the precision and accuracy of the SMPL to model the patient’s body geometry with respect to anthropomorphic measurements; ii) the capability of the VF to assist the teleoperation in the probe placement within the intercostal areas; iii) the efficiency of the framework in performing the protocol in terms of duration, compared to a standard teleoperation without assistance. The results demonstrate the reliability of the anatomical model and highlight that the provided support for the teleoperation is fundamental for an effective remote examination.

II. METHOD

A. Patient Body Modelling

In this section, we introduce the 3D perception pipeline for the generation of the patient-specific model. The model

is associated with a tracking algorithm that enables the generated model to mimic the patient’s movements, thus facilitating the acquisition of data that can be used in remote ultrasound scans.

1) *Volumetric Model using SMPL*: We exploited the Skinned Multi-Person Linear (SMPL) model [17] for the body parametrisation, which is a linear 3D model of the human body. SMPL is learnt from thousands of 3D body scans and features 3 models: male, female, and neutral. The model pose is described by 24 body joint positions $\theta \in \mathbb{R}^{3 \times 24}$ plus the body translation, while the body shape is described by 10 parameters $\beta \in \mathbb{R}^{10}$. Each θ_i , $i = 1, \dots, 23$, represents the 3D orientation of a human joint with respect to its kinematic parent, while θ_0 is reserved for the global orientation. We predicted the position (landmarks) and local orientation of each joint of the patient by means of a skeleton tracker, which provided us with the orientation of the body joints. These joint orientations were used for a rough initialisation of the SMPL model. Then, we measured a point cloud of the scene with a RGB-D stereo-camera, and we filtered the points belonging to the patient leveraging a human segmentation neural network (YOLOv8-seg). We kept just the points relative to the RGB image pixels belonging to the mask computed by the network. Consequently, we optimised with two separate processes the pose and shape parameters of the SMPL model to fit the point cloud points and landmarks. In particular, we employed the chamfer distance in combination with gradient descent to refine the initial transform of the model, i.e. θ_0 and the position. Next, we optimised θ_i , $i = 1, \dots, 21$ ignoring the hands, by reducing the error between the 3D position of the key points detected by the skeleton tracker and the SMPL joint positions. Finally, we minimised the chamfer distance again, but this time with respect to β to make the SMPL model surface overlap to the point cloud.

2) *3D Ribs Model using SKEL*: One of the recent promising biomechanical models of the human body is represented by SKEL [18], where the entire human anatomical skeleton is modelled inside the SMPL model. SKEL configuration $q \in \mathbb{R}^{46}$ is parameterised by 46 degrees of freedom, capable of modelling the anatomical complexity of the human body. The SKEL model parameters can be optimised to be aligned to a

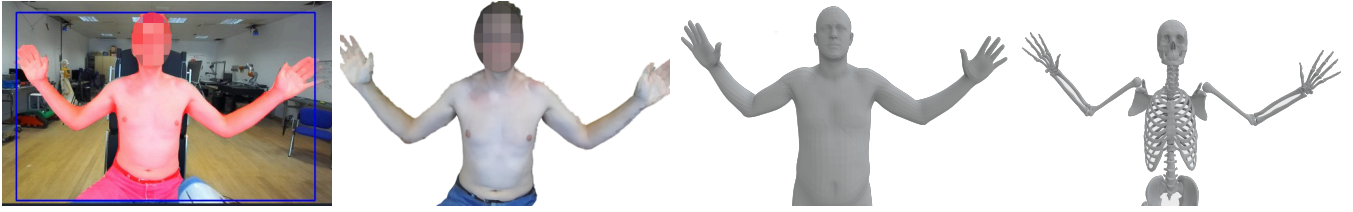


Fig. 2. Anatomical perception data and models. From left: the RGB image captured by the camera mounted at the end effector of the robot with the human segmentation provided by YOLO, the pointcloud filtered with the YOLO mask, the SMPL model, the SKEL model.

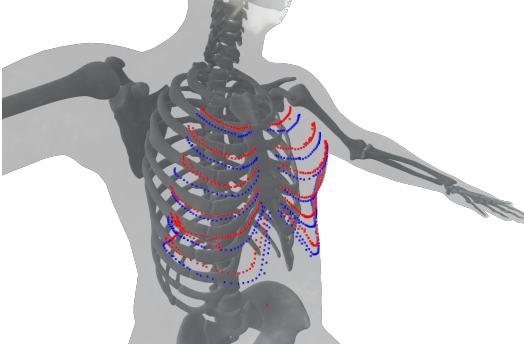


Fig. 3. The projection of ribs meshes vertices on the skinned model: superior lines are marked in red while inferior lines are marked in blue. The projected ribs are the ones involved in the lung ultrasound examination protocol.

SMPL model by minimising the mean square errors between corresponding vertices of the SMPL skin and the SKEL skin. SKEL authors also provides a measure of the average vertex fitting error with SMPL of around 1 centimetre for both male and female models. Therefore, we fitted the SKEL model to the SMPL mesh computed before to retrieve the internal skeletal model of the subject. Then we manually annotated 6 ribs per side, relevant for the lung ultrasound exam, and saved the sets of indices of the vertices of the skeletal model corresponding to the superior and inferior borders of each rib with respect to the axis of the spine. The index of a vertex $s \in \mathbb{R}^3$ of the spine in a central position is also annotated. Note that since the model is parametric, the indices are constant and always referred to the same vertices for every possible model evaluation.

With the objective in mind to constrain the interaction of the probe to the skin of the intercostal areas and avoid the bones, we developed a method to highlight, at the skin level, the presence of the ribs, beneath the skin surface. Hence, we projected every vertex belonging to the inferior and superior border sets towards the skin mesh, obtaining a cylindrical projection of those vertices. The projection direction $\mathbf{d}_{proj} \in \mathbb{R}^3$ is defined as the vector with origin in the cylinder axis passing from s and with end in the considered vertex. More formally,

$$\mathbf{d}_{proj} = \mathbf{v}_i^{y=y'} - \mathbf{s}^{y=y'} \quad (1)$$

where $\mathbf{v}_i^{y=y'} \in \mathbb{R}^3$ is the vertex of the rib i having local mesh coordinate $y = y'$, while $\mathbf{s}^{y=y'} \in \mathbb{R}^3$ is the central vertex s , but translated on the Y local mesh coordinate to achieve $y = y'$. The result of the projection can be observed in Figure 3.

Then, we interpolated the corresponding superior and inferior vertices for each rib with a cubic polynomial. After that, the central line is retrieved by averaging the superior and inferior cubic polynomials. Finally, the 3D mesh of a curved tube with an elliptical cross section is computed along the central line. The ellipsis minor axis length was defined to be proportional to the mean distance between the superior and inferior curves, with the major axis double the minor. While the dimensions of the ellipsis axes are arbitrary, we would like to highlight that the choice depends on the amount of autonomy we want to give to the human operator, which depends on his/her skills. In case of VF with larger size, the reference position is more easily constrained with respect to smaller sizes. On the other hand, with large-sized VF, potential misalignment of the model robs with the real ones might prevent the operator from placing the probe in the intercostal area. Finally, one should avoid that ellipsis belonging to different projected ribs intersect, as this would mean that the area between two ribs belongs to the forbidden region. The perception pipeline, from the camera acquisition to the skeletal model, is depicted in Figure 2.

B. Anatomical Virtual Fixtures

Once the forbidden regions are defined, they can be enforced as VF through a constraint optimisation problem, thereby preventing the ultrasound probe mounted on the robot's end effector from penetrating during the operation. As a result, the system gains robustness with respect to eventual operator errors due to faulty perception. In such a case, the reference coming from the teleoperation will be filtered and slide on top of the surface of the virtual fixture until the probe reaches the desired intercostal area. In addition, we will prevent the operator from applying high force to the ribs, potentially harming the patient. Notably, the skeletal model of the body is generated based on the patient's anatomical characteristics, resulting in the forbidden regions constructed on the ribs being tailored to the individual.

1) *Forbidden Region Enforcement*: VF are subdivided mainly into two categories: regional and guidance constraints. The former creates inaccessible areas for the robot tool, while the latter creates trajectories for the user to follow. We could have implemented guidance constraints relying on a force feedback to guide the operator, but that force would be added to the force feedback of the operator, which would potentially confuse them with the feedback generated by the contact with the environment. This was the main reason why we opted for forbidden region VF. In particular, these VF are

unilateral, and the forbidden region is defined using a mesh. The motion control of the robot end effector is formulated as a quadratic optimisation problem with linear constraints. A general formulation of the problem is the following:

$$\begin{aligned} & \arg \min_{\Delta \mathbf{x}} \|\Delta \mathbf{x} - \Delta \mathbf{x}_d\|_2, \\ & \text{subject to } \mathbf{A} \Delta \mathbf{x} \geq \mathbf{b} \end{aligned} \quad (2)$$

where $\Delta \mathbf{x} \in \mathbb{R}^3$ and $\Delta \mathbf{x}_d \in \mathbb{R}^3$ represent, respectively, the actual incremental position of the tool and the desired incremental position of the tool. The linear constraints are defined through the matrices $\mathbf{A} \in \mathbb{R}^{n \times 3}$ and $\mathbf{b} \in \mathbb{R}^n$ with n the number of constraints.

The rationale behind expressing the problem as a quadratic minimisation problem is that the forbidden zones can be defined by multiple walls which are described by hyper-planes with normal $\mathbf{n} \in \mathbb{R}^3$ and a point $\mathbf{p} \in \mathbb{R}^3$. This approach allows for the imposition of constraints on the movement of the tip, ensuring that only the positive part of the hyper-plane is admissible. Said $d_t \in \mathbb{R}$ the absolute value of the distance between the plane and the tooltip at an instant $t \in \mathbb{R}^3$, $\Delta d \in \mathbb{R}^3$ the change of the signed distance and \mathbf{x} the current end effector position, we get

$$\begin{aligned} d_{t-1} &= \mathbf{n}^\top (\mathbf{x} - \mathbf{p}) \\ \Delta d &= \mathbf{n}^\top \Delta \mathbf{x} \\ d_t &= d_{t-1} + \Delta d \geq 0 \\ \mathbf{n}^\top \Delta \mathbf{x} &\geq -\mathbf{n}^\top (\mathbf{x} - \mathbf{p}). \end{aligned} \quad (3)$$

The linear constraint of the quadratic problem (2) can be obtained by selecting $\mathbf{A} = \mathbf{n}^\top$ and $\mathbf{b} = -\mathbf{n}^\top (\mathbf{x} - \mathbf{p})$. We added a small modification to this constraint to account for the shape of the ultrasound probe. We approximated the ultrasound probe contact surface with a sphere of radius r . Therefore, we can rewrite \mathbf{b} as

$$\mathbf{b} = -\mathbf{n}^\top (\mathbf{x} - \mathbf{p}) + r \quad (4)$$

which ensures us that the probe stays out of the forbidden area. In the following subsection, we will explain how the constraint optimisation problem was solved in case of VF described by meshes.

2) *Mesh-Based Polygon Constraint Optimisation:* Li et al. [20] showed that it is possible to consider only a part of a mesh to build the optimisation problem. A sphere is defined within which all positions attainable by the robot end effector, $\mathbf{x} \in \mathbb{R}^3$, in a control cycle are contained. The mesh triangles within this sphere account for the motion constraint. For each triangle, the point at which the distance between the end effector and the plane defined by the triangle is minimum is determined, defined as the *closest point* and dubbed $\mathcal{CP} \in \mathbb{R}^3$. If the \mathcal{CP} is located within the triangle, no alterations are required. Conversely, if the \mathcal{CP} is positioned outside the triangle, it is necessary to project it onto the edge of the triangle. Subsequently, the planes must be incorporated as active constraints into the minimisation problem. The plane normals added to the row of the constraint matrix \mathbf{A}

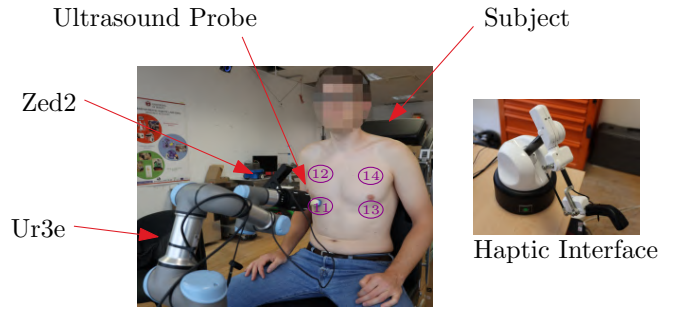


Fig. 4. Experimental setup. (left) remote system and the subject, (right) haptic interface used by the physician. In purple are shown the areas of the lung ultrasound acquisitions according to the protocol [1]. A video of the experiment is available at <https://youtu.be/ULzPU-DwWxk>.

are determined by the location of \mathcal{CP}_i accounting for these cases:

- 1) **Condition 1:** The \mathcal{CP}_i is in the triangle and \mathbf{x} is the positive side of the face normal \mathcal{N}_i . The plane having normal $\mathcal{N}_i - \mathcal{CP}_i$ is added to the constraints.
- 2) **Condition 2:** The \mathcal{CP}_i is on the edge of the triangle and the local surface described by the considered triangle and the adjacent triangle which shares \mathcal{CP}_i is convex. The plane having normal $\mathbf{x} - \mathcal{CP}_i$ is added to the constraints.
- 3) **Condition 3:** The \mathcal{CP}_i is on the edge of the triangle, \mathbf{x} is on the positive side of the face normal \mathcal{N}_i and the local surface described by the considered triangle and the adjacent triangle which shares \mathcal{CP}_i is concave. The plane having normal $\mathcal{N}_i - \mathcal{CP}_i$ is added to the constraints.

C. Robot Interaction Control

In the context of human-robot interaction and teleoperation, Cartesian impedance control is widely employed due to the possibility to modulate the amount of force exerted from the robot to the environment while tracking Cartesian trajectories [21]–[23]. This type of control enables the robot's end effector to behave as a mass-spring-damper system. In particular, the amount of force generated depends on the offset between the desired position and the robot's actual position. Given \mathbf{F}_{ee}^{ext} the interaction force between the robot's end effector and the environment, the closed loop behaviour is described by:

$$\Lambda_d \ddot{\tilde{\mathbf{x}}_{ee}} + \mathbf{D}_d \dot{\tilde{\mathbf{x}}_{ee}} + \mathbf{K}_d \tilde{\mathbf{x}}_{ee} = \mathbf{F}_{ee}^{ext}, \quad (5)$$

where $\tilde{\mathbf{x}}_{ee} = \mathbf{x}_d - \mathbf{x}_{ee} \in \mathbb{R}^m$ defines the Cartesian position error, \mathbf{x}_d the desired position, $\Lambda_d \in \mathbb{R}^{m \times m}$ the desired inertia, $\mathbf{D}_d \in \mathbb{R}^{m \times m}$ the damping and $\mathbf{K}_d \in \mathbb{R}^{m \times m}$ the stiffness. In this formulation the measurement of the force by the force/torque sensor is necessary. Imposing the desired inertia to be equal to the inertial matrix of the end effector, $\Lambda_d = \Lambda(\mathbf{x})$ is possible to avoid the feedback of the sensor [24].

III. EXPERIMENTS

The proposed telehealth system is divided into two main sites (the setup is available in Figure 4). At the patient's side (follower), a collaborative robot endowed with force/torque

sensing at the end effector and an ultrasound probe is in charge of the physical examination. The robot is teleoperated remotely by a physician by means of a haptic interface (leader), which sends the desired pose to the follower and renders its physical interaction with the environment (the patient’s body) through the interface force feedback. Two RGB-D cameras, one mounted at the robot end-effector and the other fixed on a tripod, monitor the robot action and broadcasts its information to the physician’s GUIs, which consist, alternatively, of a standard video or a virtual reality interface, that replicates the patient’s environment. The haptic device is a Haption Desktop 6D, which ensures 6 DoFs, plus force and torque feedback and run at 1 khz. The manipulator is a 6 DoFs UR3e controlled at 500 hz with an integrated 6-axis F/T sensor mounted at the robot’s end-effector. The robot is controlled with a Forward Dynamics Compliance controller [25] which renders an impedance behaviour on kinematically controlled robots. The controller parameters are the following: stiffness $K_{i,i} = 1000, i = 0, \dots, 2$ and $K_{i,i} = 20, i = 3, \dots, 5$, damping $D_{i,i} = 2\sqrt{K_{i,i}}$, inner PD force controller gains $k_p = 0.05$ and $k_d = 0.005$ for the translation and $k_p = 1.5$ for the rotation, to ensure the force tracking. The RGB-D sensors are a Zed 2 stereo camera mounted on the robot end effector for the 3D model generation and a RealSense 435i fixed on the tripod for the 2D visual feedback. As end-effector tool we integrated the ATL Wi-Fi US Probe which is attached to the robot flange with a 3D-printed support. We used qpOASES [26] to solve the mesh-based polygon constraint QP. The radius r of the probe was set to 1 centimetre. The software components of the framework were communicating through ROS2 Humble installed on Ubuntu 22.04 running on a computer with an AMD Ryzen 9 5900X (24) @ 3.7 GHz \times 12-cores CPU, 32 GB RAM, and NVIDIA RTX 4070 GPU.

A. Validation of the Body Model Customisation

Since the quality of the skeletal model fitting is strictly related to the SMPL parameters prediction, we evaluated the precision and the accuracy of the algorithm, highlighting the capability of the optimisation of the SMPL model to adapt to different subjects. We considered 3 anthropometric measurements, which are related to the body area of interest of this paper: 1) chest circumference (CC), 2) waist circumference (WC), and 3) shoulder to crotch height (SCH). First, we evaluated the repeatability of the body estimation pipeline by computing the mean and standard deviation of the anthropometric measurements in 10 reconstructions for the same volunteer. The measurements, obtained with the utility SMPL-Anthropometry [27], were then compared with the actual measurements taken from the patient’s body with a measuring tape (as in medical visits). The measures, expressed in metres, are reported in Table I. As we can notice, we obtained an acceptable standard deviation for our task, especially in the case of CC, which is also the most relevant among the 3 since it is measured near the scanning areas: in this case, the standard deviation is approximately of 3 cm, which embeds also the low accuracy and precision of the ground truth

TABLE I
SINGLE SUBJECT ANTHROPOMETRIC MEASUREMENTS [M] (10 SAMPLES)

MEASUREMENT	SMPL (MEAN \pm STD)	MEASURE TAPE
CC	0.964 \pm 0.034	0.955
WC	0.944 \pm 0.054	0.885
SCH	0.664 \pm 0.030	0.621

TABLE II
ANTHROPOMETRIC MEASUREMENTS ERRORS [M] (SINGLE SAMPLE)

SUBJECT	CC ERROR	WC ERROR	SCH ERROR
1	0.013	-0.001	0.040
2	-0.081	-0.057	-0.029
3	-0.017	0.015	0.024
4	0.045	0.140	-0.036

measurement method. Then we compared the tape-based measurements with the anthropometric measurements given by the SMPL model for 4 male volunteers (only the male SMPL model is considered), height of 1.83 ± 0.05 metres and mass of 88 ± 8 kilograms. The differences between the SMPL and the actual measurements are shown in Table II. Notice that, again, we obtained reasonably low differences, comparable with the ground truth measurements errors, and with the only exception of CC in patient 2 and WC in patient 4 where outliers can be observed.

B. Validation of the Virtual Fixtures Strategy

To validate the effectiveness of the VF, a lung ultrasound was performed in the areas of the right basal on mid-clavicular line below the internipple line (area 11) and of the right upper on mid-clavicular line above the internipple line (area 12), as proposed by Soldati et al. [1] for the standardisation of this examination (see Figure 4). During the examination, the operator, controlling the robot with the haptic interface, approaches the intercostal space based solely on the images provided by the RGB camera and the rib reconstruction on the skinned model. We would like to point out that the presence of the 3D visual feedback, which includes the fixtures, highly contributes to assist the physician in reaching the intercostal space, thereby avoiding the placement of the probe on the bone and the subsequent need for acquisition correction. In Figure 5, depicting the outcome of this test, the reference trajectory is generated by the haptic interface, the constrained trajectory is the trajectory with the VF enforcement, and the current trajectory is the position of the robot end effector. With these results, it is possible to observe the activation of the VF in the presence of a mismatch between the reference and the constrained trajectory.

C. Overall Validation with Lung Ultrasound Protocol

In light of the challenges associated with the objective assessment of the influence of VF on the acquisition of ultrasound images and the lack of image-based metrics to evaluate the quality of such images, the advantages of the proposed methodology were evaluated based on the duration

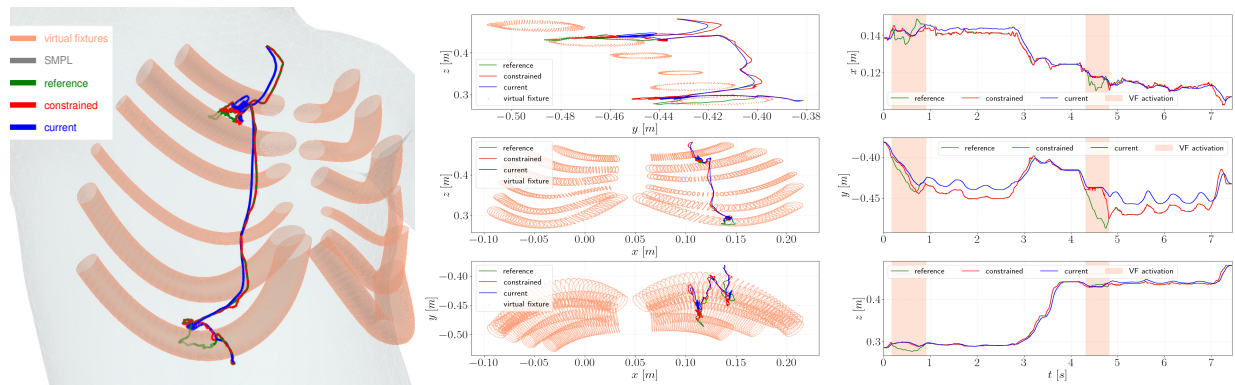


Fig. 5. Plots of experiment in subsection III-B. (left) 3D plot, (middle) 2D slices of the 3D plot, (right) variables over time.

TABLE III
MEAN EXAMINATION DURATION [s] WITH AND WITHOUT THE
PROPOSED SHARED CONTROL FRAMEWORK

EXPERIMENT	w/ VF, MEAN \pm STD	w/o VF, MEAN \pm STD
2-pts, operator #1	35 \pm 8	50 \pm 13
4-pts, operator #2	100 \pm 15	135 \pm 9

of the examinations. Before performing the 4-points frontal examination in accordance with the methodology delineated by Soldati et al. [1] (see Figure 4), we performed a study with only 2 points: 11 and 12, similarly to the second experiment. The acquisition was deemed valid at each point if the pleural line was visible for a minimum of 90% of its horizontal extension in the image (see Figure 6 for a visual reference). Before the experiment starts, the operator tested for 10 minutes the system to become acquainted with it and to avoid the introduction of any bias into the initial measurements. Furthermore, the tests with and without VF were alternated, to prevent major influence due to the indirect training of the task from the subject with a total of 10 attempts (5 with VF and 5 without). The mean and standard deviation (in seconds) of the error between the examination with and without the VF for the 2-points study with operator #1 are reported in the first row of Table III.

Data shows a marked reduction of 30% in the total execution time of the examination when the VF were used and lower standard deviation, indicating higher repeatability. We then extended this experiments by performing the 4-points examination (areas 11-12-14-13) with the same modalities. To further reduce the bias, we also change the operator. The 4-points protocol mean and standard deviation duration times with and without our assistance method for operator #2 are reported in the second row of Table III. As we can observe, the total time was reduced by approximately 26%, comparable with the 2-points attempts with a different operator. Overall, the 2-points and 4-points evaluations remark a promising improvement in the total execution time.

Furthermore, the operators reported a reduced cognitive effort and an increased confidence during free motion, attributed to the easier identification of target points. Another limitation identified by the user when relying solely on the RGB image for feedback is the occlusion of the camera

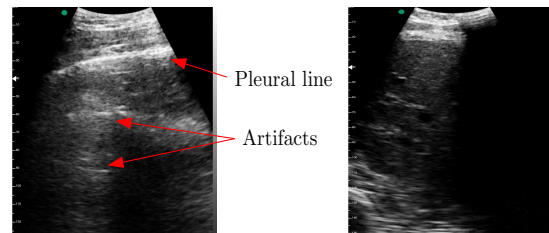


Fig. 6. Examples of lung ultrasound images sampled from the probe attached at the end effector of the robot. (left) full pleural line (right) rib shadow.

view by the end effector in certain configurations, which complicates the interaction process. This issue, however, was not critical when VF were employed, since, thanks to the 3D visual feedback, the position of the probe in the ribs region remained consistently visible.

IV. CONCLUSIONS

In this work, we addressed the problem of patient specificity mainly for the context of robotised lung ultrasound. Through a model that embeds the pose and the shape of the human body, we were able to generate an anatomical skeleton. We then implemented an automatic way of generating VF from the skeletal model, and we used them to constrain the physical interaction to the intercostal areas. The framework has been validated in quantitative experiments: at first, we measured the repeatability and generalisation capability of the body modelling approach; secondly, we evaluated the impact of the VF in the examination by monitoring the execution time of the 2 and 4 frontal areas of a clinically validated ultrasound protocol. Results shows higher-than-acceptable body modelling repeatability, while patient subjectivity is taken in due consideration. The ultrasound protocol was executed faster with the VF, indicating a promising research direction. Potential future work includes the integration of real-time measurements, such as contact force, to enhance the body model with viscoelastic properties, e.g., [23], and to compensate for the limitations of vision-based approach. We also plan to conduct further studies involving multiple clinicians and a larger pool of subjects.

REFERENCES

- [1] G. Soldati, A. Smargiassi, R. Inchingolo, D. Buonsenso, T. Perrone, D. F. Briganti, S. Perlini, E. Torri, A. Mariani, E. E. Mossolani, F. Tursi, F. Mento, and L. Demi, "Proposal for International Standardization of the Use of Lung Ultrasound for Patients With COVID-19," *Journal of Ultrasound in Medicine*, vol. 39, no. 7, pp. 1413–1419, 7 2020.
- [2] L. Demi, F. Wolfram, C. Klersy, A. De Silvestri, V. V. Ferretti, M. Muller, D. Miller, F. Feletti, M. Welnicki, N. Buda, A. Skoczylas, A. Pomiecko, D. Damjanovic, R. Olszewski, A. W. Kirkpatrick, R. Breikreutz, G. Mathis, G. Soldati, A. Smargiassi, R. Inchingolo, and T. Perrone, "New International Guidelines and Consensus on the Use of Lung Ultrasound," *Journal of Ultrasound in Medicine*, vol. 42, no. 2, pp. 309–344, 2 2023.
- [3] J. Wang, C. Peng, Y. Zhao, R. Ye, J. Hong, H. Huang, and L. Chen, "Application of a Robotic Tele-Echography System for COVID-19 Pneumonia," *Journal of Ultrasound in Medicine*, vol. 40, no. 2, pp. 385–390, 2 2021.
- [4] R. Ye, X. Zhou, F. Shao, L. Xiong, J. Hong, H. Huang, W. Tong, J. Wang, S. Chen, A. Cui, C. Peng, Y. Zhao, and L. Chen, "Feasibility of a 5G-Based Robot-Assisted Remote Ultrasound System for Cardiopulmonary Assessment of Patients With Coronavirus Disease 2019," *Chest*, vol. 159, no. 1, pp. 270–281, 1 2021.
- [5] R. Tsumura, J. W. Hardin, K. Bimbraw, A. V. Grossestreuer, O. S. Odusanya, Y. Zheng, J. C. Hill, B. Hoffmann, W. Soboyejo, and H. K. Zhang, "Tele-Operative Low-Cost Robotic Lung Ultrasound Scanning Platform for Triage of COVID-19 Patients," *IEEE Robotics and Automation Letters*, vol. 6, no. 3, pp. 4664–4671, 7 2021.
- [6] L. Al-Zogbi, V. Singh, B. Teixeira, A. Ahuja, P. S. Bagherzadeh, A. Kapoor, H. Saedi, T. Fleiter, and A. Krieger, "Autonomous Robotic Point-of-Care Ultrasound Imaging for Monitoring of COVID-19–Induced Pulmonary Diseases," *Frontiers in Robotics and AI*, vol. 8, p. 645756, 5 2021.
- [7] J. Tan, B. Li, Y. Leng, Y. Li, J. Peng, J. Wu, B. Luo, X. Chen, Y. Rong, and C. Fu, "Fully Automatic Dual-Probe Lung Ultrasound Scanning Robot for Screening Triage," *IEEE Transactions on Ultrasonics, Ferroelectrics, and Frequency Control*, vol. 70, no. 9, pp. 975–988, 9 2023.
- [8] B. Zhang, H. Cong, Y. Shen, and M. Sun, "Visual Perception and Convolutional Neural Network-Based Robotic Autonomous Lung Ultrasound Scanning Localization System," *IEEE Transactions on Ultrasonics, Ferroelectrics, and Frequency Control*, vol. 70, no. 9, pp. 961–974, 9 2023.
- [9] Y. Fu, W. Lin, X. Yu, J. J. Rodriguez-Andina, and H. Gao, "Robot-assisted teleoperation ultrasound system based on fusion of augmented reality and predictive force," *IEEE Transactions on Industrial Electronics*, vol. 70, pp. 7449–7456, 7 2023.
- [10] D. Huang, C. Yang, M. Zhou, A. Karlas, N. Navab, and Z. Jiang, "Robot-assisted deep venous thrombosis ultrasound examination using virtual fixture," *IEEE Transactions on Automation Science and Engineering*, pp. 1–12, 2024.
- [11] M. Shahbazi, S. F. Atashzar, and R. V. Patel, "A dual-user teleoperated system with Virtual Fixtures for robotic surgical training," in *2013 IEEE International Conference on Robotics and Automation*, May 2013, pp. 3639–3644, iSSN: 1050-4729.
- [12] S. A. Bowyer, B. L. Davies, and F. Rodriguez y Baena, "Active Constraints/Virtual Fixtures: A Survey," *IEEE Transactions on Robotics*, vol. 30, no. 1, pp. 138–157, Feb. 2014, conference Name: IEEE Transactions on Robotics.
- [13] A. Bettini, P. Marayong, S. Lang, A. Okamura, and G. Hager, "Vision-assisted control for manipulation using virtual fixtures," *IEEE Transactions on Robotics*, vol. 20, no. 6, pp. 953–966, 2004.
- [14] R. Moccia, C. Iacono, B. Siciliano, and F. Ficuciello, "Vision-Based Dynamic Virtual Fixtures for Tools Collision Avoidance in Robotic Surgery," *IEEE Robotics and Automation Letters*, vol. 5, no. 2, pp. 1650–1655, Apr. 2020, conference Name: IEEE Robotics and Automation Letters.
- [15] F. Rydén and H. J. Chizeck, "Forbidden-region virtual fixtures from streaming point clouds: Remotely touching and protecting a beating heart," in *2012 IEEE/RSJ International Conference on Intelligent Robots and Systems*, Oct. 2012, pp. 3308–3313, iSSN: 2153-0866.
- [16] H. Oğul, B. B. Oğul, A. M. Ağildere, T. Bayrak, and E. Sümer, "Eliminating rib shadows in chest radiographic images providing diagnostic assistance," *Computer Methods and Programs in Biomedicine*, vol. 127, pp. 174–184, 2016.
- [17] M. Loper, N. Mahmood, J. Romero, G. Pons-Moll, and M. J. Black, "SMPL: A skinned multi-person linear model," *ACM Trans. Graphics (Proc. SIGGRAPH Asia)*, vol. 34, no. 6, pp. 248:1–248:16, Oct. 2015.
- [18] M. Keller, K. Werling, S. Shin, S. Delp, S. Pujades, C. K. Liu, and M. J. Black, "From skin to skeleton: Towards biomechanically accurate 3D digital humans," *ACM Transaction on Graphics (ToG)*, vol. 42, no. 6, pp. 253:1–253:15, Dec. 2023.
- [19] G. Jocher, A. Chaurasia, and J. Qiu, "Ultralytics yolov8," 2023. [Online]. Available: <https://github.com/ultralytics/ultralytics>
- [20] Z. Li, A. Gordon, T. Looi, J. Drake, C. Forrest, and R. H. Taylor, "Anatomical mesh-based virtual fixtures for surgical robots," in *2020 IEEE/RSJ International Conference on Intelligent Robots and Systems (IROS)*, 2020, pp. 3267–3273.
- [21] E. Sartori, C. Tadiello, C. Secchi, and R. Muradore, "Tele-echography using a two-layer teleoperation algorithm with energy scaling," *Proceedings - IEEE International Conference on Robotics and Automation*, vol. 2019-May, pp. 1569–1575, 5 2019.
- [22] M. Selvaggio, G. A. Fontanelli, F. Ficuciello, L. Villani, and B. Siciliano, "Passive virtual fixtures adaptation in minimally invasive robotic surgery," *IEEE Robotics and Automation Letters*, vol. 3, no. 4, pp. 3129–3136, 2018.
- [23] L. Beber, E. Lamon, D. Nardi, D. Fontanelli, M. Saveriano, and L. Palopoli, "A passive variable impedance control strategy with viscoelastic parameters estimation of soft tissues for safe ultrasonography," *2024 IEEE International Conference on Robotics and Automation (ICRA)*, pp. 1298–1304, 5 2024.
- [24] A. Dietrich, X. Wu, K. Bussmann, M. Harder, M. Iskandar, J. Engelsberger, C. Ott, and A. Albu-Schäffer, "Practical consequences of inertia shaping for interaction and tracking in robot control," *Control Engineering Practice*, vol. 114, p. 104875, 9 2021.
- [25] S. Scherzinger, A. Roennau, and R. Dillmann, "Forward dynamics compliance control (fdcc): A new approach to cartesian compliance for robotic manipulators," in *IEEE/RSJ International Conference on Intelligent Robots and Systems (IROS)*, 2017, pp. 4568–4575.
- [26] H. J. Ferreau, C. Kirches, A. Potschka, H. G. Bock, and M. Diehl, "qpOASES: a parametric active-set algorithm for quadratic programming," *Mathematical Programming Computation*, vol. 6, no. 4, pp. 327–363, Dec. 2014. [Online]. Available: <https://doi.org/10.1007/s12532-014-0071-1>
- [27] D. Boja, "Smpl anthropometry," 2023. [Online]. Available: <https://github.com/DavidBoja/SMPL-Antropometry/>